Materials Science in Semiconductor Processing 180 (2024) 108565

Contents lists available at ScienceDirect

Materials Science in Semiconductor Processing

journal homepage: www.elsevier.com/locate/mssp

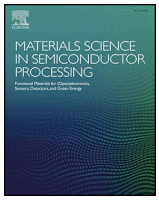

Determination of the indirect bandgap of lattice-matched SiGeSn on Ge

Daniel Schwarz [a,*], Erich Kasper [a], Florian Bärwolf [b], Ioan Costina [b], Michael Oehme [a]

[a] Institute of Semiconductor Engineering (IHT), University of Stuttgart, Pfaffenwaldring 47, 70569, Stuttgart, Germany
[b] IHP - Leibniz-Institute High Performance Microelectronics, Im Technologiepark 25, 15236, Frankfurt (Oder), Germany

ARTICLE INFO

Keywords:
Silicon germanium tin
Molecular beam epitaxy
Bandgap determination
Capacitance voltage measurement

ABSTRACT

The first experimental results for the indirect bandgap of SiGeSn, lattice-matched on Ge are reported. The necessary condition for lattice-matching on Ge is a constant ratio of Si/Sn = 3.67. Thus, the investigated composition range is $c_{Sn} = \{5.0, 7.5, 10.0\}$ % and precisely investigated using secondary ion mass spectroscopy. The bandgap determination is based on the extraction of the built-in voltage of a SiGeSn pn^{++} junction utilizing the so-called capacitance-voltage intercept method. Detailed calculations of the band diagram of the pn^{++} junction to be investigated, including first level approximations for the effective density of states in the valence and conduction band were performed. The results show that the composition of the alloy strongly influences its bandgap and is $E^{L}_{g,SiGeSn} = \{0.588, 0.704, 0.413\}$ eV, respectively.

1. Introduction

In recent years, the ternary alloy semiconductor silicon germanium tin (SiGeSn) has experienced an increasing interest due to its unique properties in the field of group IV alloy semiconductors. On top of being a direct bandgap semiconductor at specific compositions and strain, it also allows the growth of strain-free heterostructures on the Si platform. SiGeSn thus opens up a wide range of interesting application possibilities, such as the Si integrated laser light source [1–3], the tunneling field effect transistor (TFET) [4,5] or even multi-quantum well devices like quantum cascade lasers [6].

However, despite its numerous advantages, the growth of high-quality SiGeSn proves itself quite challenging due to the limited solid solubility of Sn in Ge and Si of less than one percent. Besides, the novelty of the material system implies that only a few material parameters have been precisely experimentally determined. An example is the composition dependent indirect and direct bandgap. Especially the indirect bandgap of lattice matched SiGeSn on Ge has been determined only simulative by now. However, its knowledge is crucial for the design of actual heterostructures and therefore to bring this material into its application.

In this paper, we present the first experimental determination of the indirect bandgap of lattice matched SiGeSn on Ge. To this end, we performed capacitance-voltage (CV) measurements on SiGeSn pin diodes grown by molecular beam epitaxy (MBE). Discrete diode devices were fabricated out of the MBE grown layers using a standard single mesa process which is compatible to complementary metal oxide semiconductor (CMOS) technology. The indirect bandgap was extracted from the CV measurements using the CV intercept method [7,8]. However, this also requires the knowledge of the Fermi level positions in the doped regions. Therefore, we also present a first approximation of the effective densities of states in the valence and conduction band, respectively. Since we present in this work experimental data for the indirect bandgap of SiGeSn in dependence of its composition, we also determined the actual alloy composition of the SiGeSn layers. Here we performed secondary ion mass spectroscopy (SIMS), which gives not only an integral information of the alloy composition but also information about the alloy uniformity along the growth direction. Besides that, the results of the SIMS analysis reveal the actual doping concentration as well as the doping profiles.

2. Sample fabrication

All investigated device layer stacks, as seen in Fig. 1, were grown with a 6-inch MBE system, where Si, Ge and Sn are used as matrix materials and B and Sb as dopants respectively. Since the substrate temperature T_S is the most important growth parameter especially for Sn containing group IV alloys, its measurement and control was performed using two different methods, depending on its operating regime. For the temperature growth regime of $T_S \geq 250°C$, a carefully calibrated thermocouple, located behind the substrate heater, was used. However, as we previously reported, this method lacks the capability to observe the

* Corresponding author.
E-mail address: daniel.schwarz@iht.uni-stuttgart.de (D. Schwarz).

https://doi.org/10.1016/j.mssp.2024.108565
Received 25 December 2023; Received in revised form 22 May 2024; Accepted 23 May 2024
Available online 27 May 2024

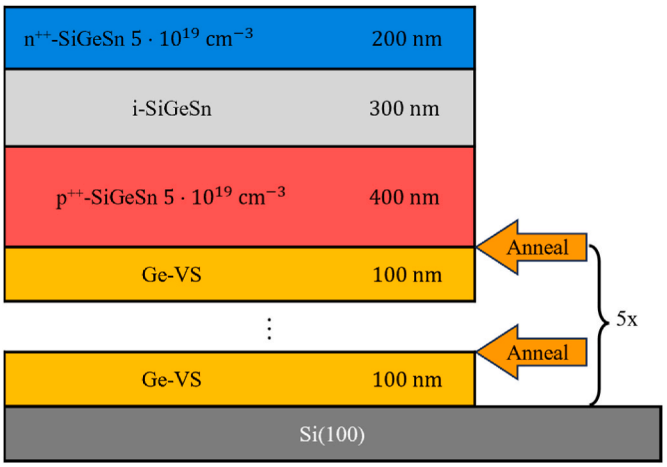

Fig. 1. MBE layer stack of the SiGeSn pin diodes on Si.

actual processes on the substrate surface in the low temperature growth regime at $T_S < 250°C$ [9]. Therefore, a mid-infrared (MIR) pyrometer with a spectral responsivity of 8 $\mu m \leq \lambda \leq 13$ μm was used in this regime to improve the epitaxy of the SiGeSn. All samples are based on moderately p-type doped Si(001) substrates with a specific sheet resistance of 10 $\Omega cm \leq \rho \leq 20$ Ωcm. The epitaxy process was initiated with a thermal desorption step at a substrate temperature for $t = 5$ min to desorb the native SiO_2 [10]. Subsequently, a Si buffer layer with $d = 50$ nm was grown at $T_S = 600°C$ to smoothen the surface.

Afterwards, the growth process continues with a Ge layer with $d = 100$ nm at $T_S = 330°C$, which was then annealed at $T_S = 830°C$ for $t = 5$ min to form a virtual substrate (VS) [11]. To achieve a further decrease of the threading dislocation density and consequently a better crystal quality of the following actual device, the VS sequence was repeated a total of five times.

In total, three different samples *5.0Sn*, *7.5Sn* and *10.0Sn* with varying composition of the SiGeSn layers, according to Table 1, were grown. In order to achieve the mentioned lattice matching on Ge, a constant ratio of the Si to Sn of $c_{Si}/c_{Sn} = 3.67$ was fulfilled via careful calibration and fixation of the respective fluxes beforehand of the actual sample growth. The variation of the SiGeSn composition was then performed by a variation of the Ge flux. Consequently, the total SiGeSn growth rate varied in the range of 1.25 Å$\cdot s^{-1} \leq R_{SiGeSn} \leq 2.50$ Å$\cdot s^{-1}$. In advance of the beginning of the SiGeSn layer growth, the substrate temperature was lowered to $T_S = 200°C$. Although the MIR pyrometer can better measure the actual surface temperature, its signal is being influenced by emissivity variations, especially during the growth of doped structures, such as the pin diode. Therefore, the heating power of the substrate was fixed to a certain value after the growth of the SiGeSn bottom layer.

The SiGeSn pin diode stack consists of a p-type doped bottom layer with $d = 400$ nm and an acceptor concentration of $N_A = 5 \cdot 10^{19}$ cm^{-3}, followed by an undoped layer with $d = 300$ nm and closed with an n-type doped top layer with $d = 200$ nm and a donor concentration of $N_D = 5 \cdot 10^{19}$ cm^{-3}.

After the layer growth via MBE, discrete pin diodes were fabricated with a single mesa process using a Si compatible standard cleanroom technology, as described as follows. First, a circular mesa structure was defined using a standard optical lithography step and a subsequent dry etch step via inductively coupled plasma reactive ion etching (ICP-RIE) with hydrogen bromide as etchant. The mesa surface was then passivated with a SiO_2 with $d = 300$ nm, deposited via plasma enhanced chemical vapor deposition at $T_S = 200°C$ with tetraethyl orthosilicate and oxygen as precursors. To enable the contact of the semiconductor regions, oxide windows were defined via reactive ion etching with fluoroform as etchant.

Prior to the contact formation, the native semiconductor oxide was removed using a sequence of successive etching steps in hydrofluoric acid with 2.5 % for a duration of t = 10 s, hydrochloric acid with 9 % for a duration of t = 30 s and intermediate as well as a final rinsing steps in deionized water. Finally, a stack of Ti ($d_{Ti} = 50$ nm) and Al ($d_{Al} = 1.2$ μm) was deposited as metallization via DC magnetron sputtering.

A scanning electron microscopy (SEM) micrograph of a finalized device with a mesa radius of $r_M = 20$ μm can be seen in Fig. 2 a). Besides that, Fig. 2 b) shows a schematic drawing of the same device.

3. Composition and strain analysis

After the material fabrication, its actual composition was analyzed using SIMS. Moreover, SIMS allows to get a deeper insight of the alloy composite distribution in growth direction. All SIMS measurements were performed utilizing a 25 keV Bi^{1+} analyzing beam, over an area of 100·100 μm^2, while monitoring secondary ions in negative mode in a time-of-flight (ToF)-SIMS V mass spectrometer from IONTOF. The used Cs sputtering beam was kept at 1 keV impact energy, bombarding an area of 300·300 μm^2.

It needs to be considered, that the sputtering of sample *10.0Sn* ended before the actual end of the layer stack, which is why its signals end at depth of 600 nm. To determine the integral values of the alloy composition, as listed in Table 1, the concentration values of the specific alloying elements were averaged along the growth direction. The B concentration was calibrated using the signal of B^{11}–Si^{28}, normalized to the Si^{28} signal and a Si reference sample. The Sb concentration was referred to the absolute values of a previously grown calibration sample. The comparison of the actual alloy composition with the nominal alloy composition, as stated for each sample in Table 1, prove its very good agreement.

Besides that, the measurement profiles of all three samples are shown in Fig. 3. The characteristics of the alloy composites along the growth direction prove their uniform distribution, which is especially remarkable. Usually, the expected strong segregation of Sn would lead to an increasing Sn concentration along the growth direction, which is not the case here. This shows in turn the good control of the substrate temperature and thus the suppression of the Sn segregation. Furthermore, an almost perfect box profile for both doped regions can be observed, which is particularly important for the CV characterization presented here.

Furthermore, since the bandgap of a semiconductor is also influenced by its strain, we performed X-ray diffraction (XRD) measurements to determine the strain degree of the grown SiGeSn layers. However, the strain should be approx. zero due to the desired lattice-matching condition. All XRD experiments, which were performed using a Rigaku Smartlab, were used to measure the asymmetric $(\overline{2}24)$ reflection. Although these data are often displayed as reciprocal space maps, the results are converted afterwards to lattice coordinates and thus displayed as space maps in Fig. 4.

Table 1
Nominal sample composition and the respective results of the composition and strain analysis.

Nominal Composition				SIMS			XRD			
Sample	c_{Si} (%)	c_{Ge} (%)	c_{Sn} (%)	c_{Si} (%)	c_{Ge} (%)	c_{Sn} (%)	$a_{\parallel}$ (Å)	$a_{\perp}$ (Å)	a_0 (Å)	$\varepsilon_{\parallel}$ (%)
5.0Sn	18.4	76.7	5.0	17.6	77.6	4.8	5.668	5.640	5.652	0.28
7.5Sn	27.5	65.0	7.5	27.7	65.3	7.0	5.664	5.634	5.647	0.30
10.0Sn	36.7	53.3	10.0	36.8	54.3	8.9	5.666	5.628	5.644	0.37

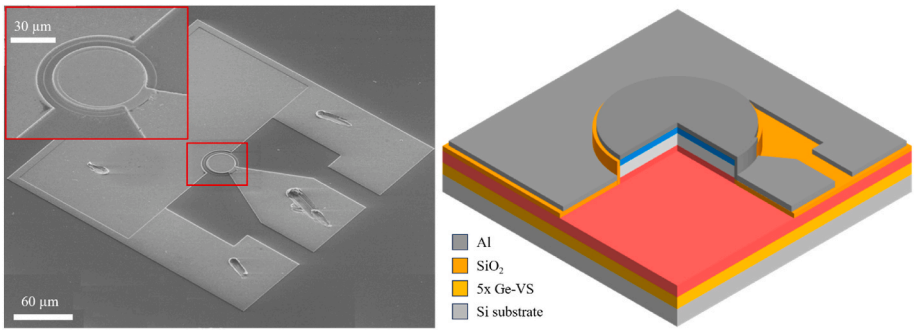

Fig. 2. a) SEM micrograph of a finalized device with a mesa diameter of $r_M = 20\,\mu m$. b) Detailed schematic drawing of a finalized device.

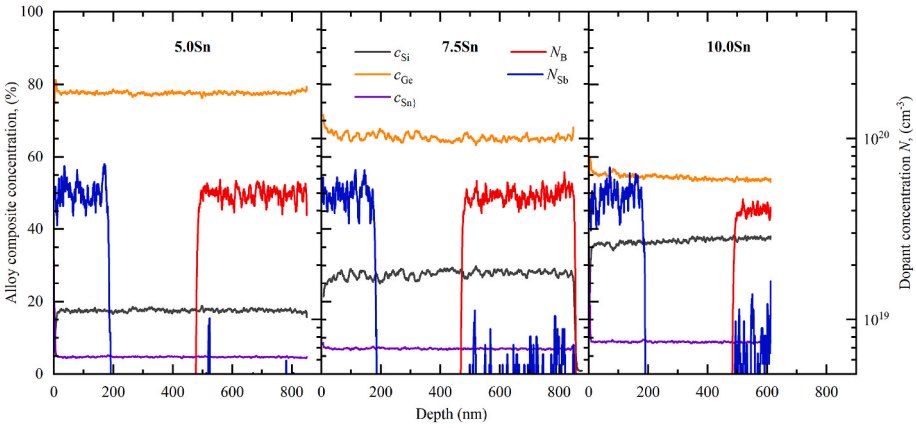

Fig. 3. SIMS concentration profiles of the alloying elements as well as the dopants for all three samples.

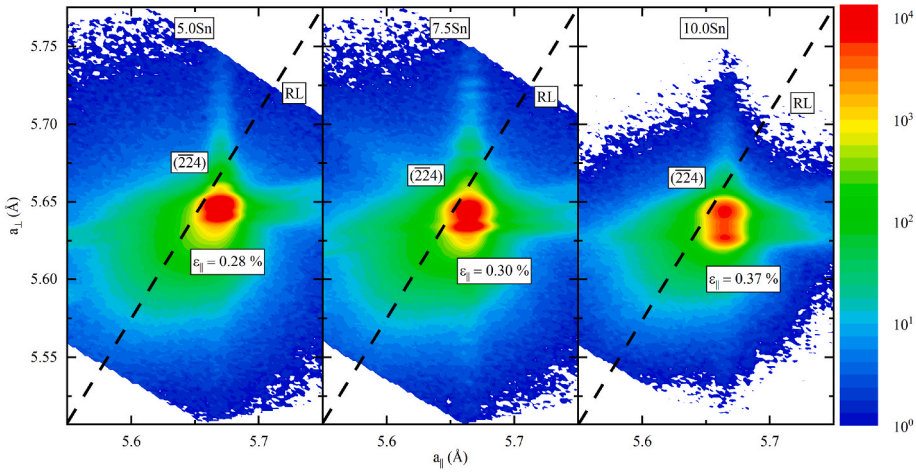

Fig. 4. XRD space maps of the asymmetric $(\overline{2}\overline{2}4)$ reflection for all three samples.

The visible dashed diagonal marks the relaxation line (RL), where all reflections above exhibit compressive strain and all reflections below exhibit tensile strain, respectively. Furthermore, the measurement results allow the extraction of the lateral lattice parameter $a_{||}$ as well as the vertical lattice parameter $a_{\perp}$. Subsequently, the relaxed lattice parameter a_0 and the residual lateral strain $\varepsilon_{||}$ were calculated using the method described in an earlier report [9]. Despite the desired lattice-matching, a residual tensile strain of the SiGeSn layers of 0.28 % $\leq \varepsilon_{\parallel} \leq$ 0.37 % is revealed. The influence of this residual strain is discussed in section 5. The results for $a_{||}$, $a_{\perp}$, a_0 and $\varepsilon_{||}$ are summarized in Table 1.

4. Electrical characterization and theory

For the static DC characterization, we used a Keithley semiconductor characterization system (SCS 4200), equipped with several source measure units (SMU) for once current voltage (IV) as well as capacitance voltage (CV) characterization. Prior to the CV characterization, IV characterization is used to investigate the proper functionality of the diodes and therefore the quality of the epitaxial layers as well as the fabrication process. Afterwards, CV characterization is used to determine the capacity of the space charge regions (SCR) of the blocking pn junction C_j in reverse direction, which is dependent on the applied bias voltage V_{DC} and its inner built-in voltage V_{bi} and follows the relationship

shown in Eq. (1), according to [7] (Eq. (25)).

$$C_j = A \cdot \sqrt{\frac{q\varepsilon_0\varepsilon_R}{2} \cdot \frac{N_A N_D}{N_A + N_D}} \cdot \frac{1}{\sqrt{V_{bi} - V_{DC} - 2V_T}} = \alpha \cdot \frac{1}{\sqrt{V_{bi} - V_{DC} - 2V_T}} \quad \text{with } V_T = \frac{k_B T}{q} \tag{1}$$

Here, A is the device area, ε_0 is the vacuum permittivity, ε_R is the relative permittivity of the semiconductor (SiGeSn) and N_A and N_D are the doping concentrations of the pn^{++} junction to be investigated. Furthermore, the thermal voltage V_T is expressed with the Boltzmann constant k_B, the Temperature T and the elementary charge q. As it can be seen, C_j is dependent on the reciprocal square-root of the applied bias with a constant pre-factor α. The further calculation of C_j^{-2} leads to a linear relationship with its axis intercept at $V_{bi} - 2V_T$ and the slope α^{-2} according to Eq. (2), which is why it is the co-called CV-intercept method.

$$C_j^{-2} = \alpha^{-2} \cdot (V_{bi} - V_{DC} - 2V_T) \tag{2}$$

However, the data must be prepared properly before the actual calculation. Due to the specific device design as shown in Fig. 2 b), the metal pad of the top contact, which lies directly on the 300 nm thick passivation oxide, forms a metal oxide semiconductor (MOS) capacity with the underlying bottom layer. This parasitic pad capacity C_{Pad} falsifies in turn the measurement of the device capacity C_D according to Eq. (3). Therefore, special so-called open structures are included on the used mask set to enable the extraction of C_{Pad}.

$$C_D = C_j + C_{Pad} \tag{3}$$

After the subtraction of C_{Pad} to get the actual value of C_j, the data needs be normalized to the device area A. Beyond that, the further calculation requires the knowledge of the doping concentrations of the semiconductor regions, which are penetrated by the SCR. These is on one hand the highly n-type doped TL, which doping concentration was carefully calibrated beforehand. On the other hand, the SCR penetrates the intrinsic region. Although it is intentionally undoped, SiGeSn exhibits, similar as it is already reported for GeSn [12], acceptor-like defect states dependent on its Sn concentration, which act as an unintentional p-type doping. Despite that, this doping concentration can be extracted from the slope of the linear characteristics of $C_j^{-2}(V)$. For this, the assumption of a strongly asymmetric pn junction with $N_D \gg N_A$ leads to the relationship shown in Eq. (4) to calculate the unintentional doping concentration $N_{A,i-SiGeSn}$.

$$N_{A,i-SiGeSn} = \frac{2}{q\varepsilon_0\varepsilon_R|\alpha^{-2}|} \tag{4}$$

The necessary relative permittivity $\varepsilon_{R,SiGeSn}$ of the SiGeSn alloy was calculated for each composition using Vegard's law [13] and the relative permittivity of Si, Ge [14] and α-Sn [15], as concluded in Table 2.

Prior to the subsequent calculation of the indirect bandgap of SiGeSn, the most dominant band transition must be determined. For this, we used the calculations from Moontragoon, Soref and Ikonic, based on empirical pseudopotential theory [16].

The compositional dependency of the three most important band transitions (Γ, L and X) of SiGeSn, lattice-matched on Ge, is shown in Fig. 5. It can be clearly seen, that SiGeSn exhibits a Ge-like band transition in the L-valley in the investigated composition range $5\,\% \leq c_{Sn} \leq 10\,\%$. Interestingly, SiGeSn, lattice-matched on Ge, shows a changeover to a Si-like semiconductor at $c_{Sn} = 11.5\,\%$, which is important for future Sn-rich investigations.

All these results together allow the bandgap calculation as a function of its composition using the band diagram of the involved pn^{++} junction as shown in Fig. 6. Here, it needs to be considered that the highly p-type doped BL acts only as a contact layer and can be neglected in the following consideration. Therefore, the indirect bandgap of SiGeSn $E_{g,SiGeSn}^{L}$ can be calculated using Eq. (5).

$$E_{g,SiGeSn}^{L} = q \cdot V_{bi} + \Delta E_{FV} - \Delta E_{FC} \tag{5}$$

$$E_{FV} = -k_B T \left[\ln\left(\frac{N_A}{N_{V,SiGeSn}}\right) + 2^{-3/2}\left(\frac{N_A}{N_{V,SiGeSn}}\right) \right] \tag{6}$$

$$E_{FC} = +k_B T \left[\ln\left(\frac{N_D}{N_{C,SiGeSn}}\right) + 2^{-3/2}\left(\frac{N_D}{N_{C,SiGeSn}}\right) \right] \tag{7}$$

The necessary energy differences between the ΔE_{FV} and ΔE_{CF} can be calculated in turn using an estimation of the Fermi-Dirac integral according to Sze for degenerated semiconductors [7] (Eq. (26a) and Eq. (26b)), as shown in Eqs. (6) and (7), respectively.

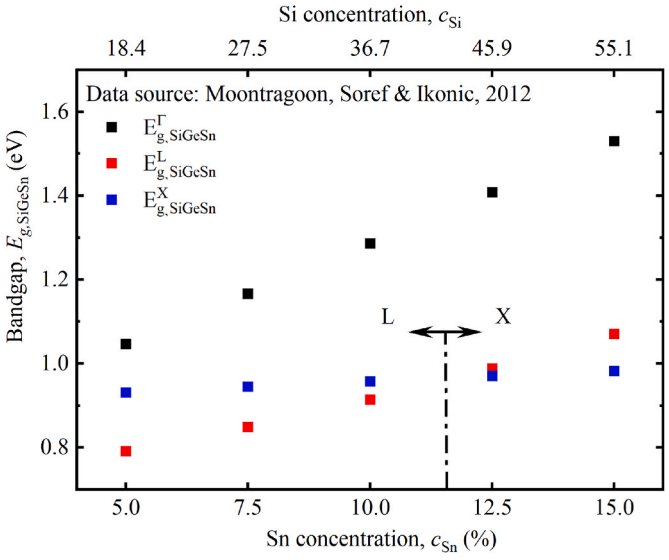

Fig. 5. Indirect and direct bandgap values of SiGeSn, lattice matched on Ge, based on the simulations by Moontragoon, Soref & Ikonic [16].

Table 2
Sample Composition and the respective approximated material data.

Nominal Composition				Effective Masses		Effective densitiy of states		Relative Permittivity
Sample	c_{Si} (%)	c_{Ge} (%)	c_{Sn} (%)	m_C	m_V	N_C (cm^{-3})	N_V (cm^{-3})	ε_R
5.0Sn	18.4	76.7	5.0	0.229	0.335	$1.10 \cdot 10^{19}$	$4.88 \cdot 10^{18}$	15.47
7.5Sn	27.5	65.0	7.5	0.236	0.361	$1.15 \cdot 10^{19}$	$5.44 \cdot 10^{18}$	15.35
10.0Sn	36.7	53.3	10.0	0.240	0.380	$1.18 \cdot 10^{19}$	$5.88 \cdot 10^{18}$	15.10
Material								
Si				0.327	0.590	$2.82 \cdot 10^{19}$	$1.14 \cdot 10^{19}$	11.7
Ge				0.220	0.294	$1.04 \cdot 10^{19}$	$4.00 \cdot 10^{18}$	15.8
α-Sn				0.024	0.058	$9.10 \cdot 10^{16}$	$3.51 \cdot 10^{17}$	24

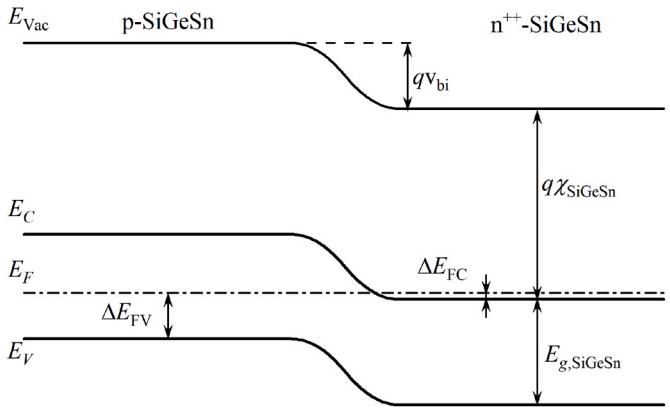

Fig. 6. Band diagram of the pn^{++} junction to be investigated.

These calculations require in turn the knowledge of the effective density of states in the valence and conduction band $N_{C,SiGeSn}$ and $N_{V,SiGeSn}$, which were calculated with Eqs. (8) and (9) according to Sze, respectively [7] (Eq. (18) and Eq. (24)), with Planck's constant h.

$$N_{C,SiGeSn} = \left(\frac{2\pi m_C k_B T}{h^2}\right)^{3/2} \cdot M_C \tag{8}$$

$$N_{V,SiGeSn} = \left(\frac{2\pi m_V k_B T}{h^2}\right)^{3/2} \tag{9}$$

For their calculation on the other hand, the values of the effective masses in the conduction and the valence band m_C and m_V are needed. Moreover, the calculation of the effective density of states in the conduction band includes the degeneracy factor M_C, which expresses the number of equivalent transitions in the conduction band. For the investigated composition range of SiGeSn, which results in a Ge-like semiconductor with the minimum in the L-valley, the degeneracy factor equals to $M_C = 4$.

The calculation of the effective mass in the conduction band of SiGeSn $m_{C,SiGeSn}$ was performed using Vegard's law of the effective masses of the alloying elements. However, for Si and Ge, literature gives only the effective masses for transversal and longitudinal movement m_t and m_l [17], respectively, which have to be transferred to m_L using Eq. (10). [7] (Eq. (15)) Besides that, the value of $m_{C,Sn}$ was taken from Ref. [18].

$$m_C = \left(m_t^2 \cdot m_l\right)^{1/3} \tag{10}$$

A similar situation is on hand for the calculation of the effective mass in the valence band of SiGeSn $m_{V,SiGeSn}$, which was also done using Vegard's law of the alloying elements. Here, for Si and Ge, the values of the effective masses for light and heavy holes m_{lh} and m_{hh} can be found in Refs. [19,20] respectively. These values were again transferred to m_V using Eq. (11) [7] (Eq. (25)). The value of $m_{V,Sn}$ was taken from Ref. [21].

$$m_V = \left(m_{lh}^{3/2} \cdot m_l\right)^{1/3} \tag{11}$$

All used values for the effective masses m_C, m_V, the effective density of states N_C and N_V and the relative permittivity ε_R of the alloying elements as well as the results for the three different alloy compositions are concluded in Table 2, which gives therefore all necessary data for the further calculation of the indirect bandgap of SiGeSn $E^L_{g,SiGeSn}$. All values in Table 2, which were calculated with Vegard's law, are based on the nominal alloy compositions for simplification.

5. Results and discussion

Directly after fabrication, the diodes were electrically characterized. In particular, the IV characteristics were measured since they serve as a proxy for crystal quality. Especially for the subsequent CV characterization, a good blocking behaviour of the pn junction is essential. The IV characterization revealed a perfect areal proportionality of the characteristics. Thus, only current density (JV) characteristics are being considered. A set of JV curves for the specific pin diodes with mesa radii of $r_M = \{5; 80\}$ μm for the varying composition according to is shown in Fig. 7.

As can be seen, the JV characteristics reveal a clear diode behaviour with an on to off current ratio of four to six orders of magnitude for the devices with $r_M = 5$ μm. However, bigger devices with $r_M = 80$ μm show a smaller on-current due to a higher on-resistance, related to the device geometry. The saturation of the on-current for $V_{DC} \geq 0.75$ V is caused by the internal compliance of the measurement setup. Despite the reduced on-current, the behaviour in reverse direction is almost identical compared to the smaller devices, which proves the good material quality. Additionally, the reverse current density shows a dependency on the alloy composition, which is a clear indication on the compositional bandgap variation. The reason for that is the proportionality of the saturation current density J_0 of an ideal pn junction on the squared intrinsic carrier concentration n_i^2, which is in turn exponentially depends on the bandgap $E^L_{g,SiGeSn}$ (see Eq. (12) [7] (Eq. (65))).

$$J_0 \propto n_i^2 \propto \exp\left(-\frac{E^L_{g,SiGeSn}}{k_B T}\right) \tag{12}$$

The reverse current density J_{-1V} at a bias voltage of $V_{DC} = -1$ V is here, dependent on the alloy composition, in the range of $30\ \text{mA}\cdot\text{cm}^{-2} \leq J_{-1V} \leq 1000\ \text{mA}\cdot\text{cm}^{-2}$, which proves a good device quality in comparison to literature [22]. A good blocking behavior is again essential for the subsequent CV characterization.

In the next step, we performed the CV characterization to measure the capacity of the SCR C_j. For this, we varied the DC bias V_{DC} in the range of $-0.8\ \text{V} \leq V_{DC} \leq 0.3$ V. The actual measurement voltage with a

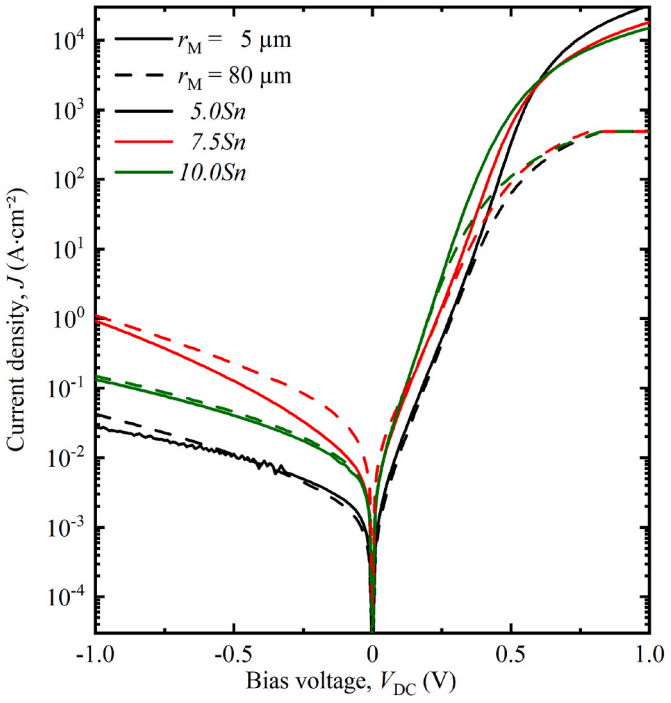

Fig. 7. IV characteristics of one exemplary SiGeSn pin diode device with a mesa radius of $r_M = 5$ µm for each composition.

frequency of $f = 100$ kHz and an amplitude of $V_{AC} = 20$ mV is modulated onto this to measure the complex impedance of the device. The measurement data was transferred assuming a parallel model of the device capacitance C_D and a conductance G_D. Afterwards, the capacity C_D was, as previously described, corrected by the value of the open structure C_{Pad}, to extract the actual value C_j of the inner pn junction, and normalized to the device area A. To determine the built-in voltage v_{bi} via linear extrapolation towards the x-axis intercept, the junction capacity C_j was then converted into C_j^{-2}. The resulting characteristics as function of the bias voltage v_{DC} for a device with $r_M = 80\,\mu$m for each alloy composition is shown in Fig. 8.

Although the data shows a clear linear behavior in the range of $-0.3\text{ V} \leq v_{DC} \leq 0.0$ V, the values start to deviate from the linear fit for lower bias voltages $v_{DC} < -0.3$ V, which is due to an increased reverse current. However, the data is perfectly suitable to extract the built-in voltage v_{bi}. The complete measurement procedure was performed for at least $n \geq 70$ devices with mesa radii $r_M = \{10, 20, 40, 80\}\,\mu$m for each alloy composition, as shown in the summarizing graph in Fig. 9.

For the calculation of the Fermi level position in the unintentionally p-type doped SiGeSn region, the acceptor-like defect state concentration $N_{A,SiGeSn}$ was determined using the slope of the linear fit α^{-2}, as seen in Fig. 8, and Eq. (4). This method was again performed for all $n \geq 70$ devices. The results are summarized in the overview in Fig. 10.

While the samples *5.0Sn* and *10.0Sn* show an acceptor-like defect concentration of $N_{A,SiGeSn} \approx 3{\cdot}10^{17}$ cm^{-3}, it is remarkably higher for sample *7.5Sn* at $N_{A,SiGeSn} \approx 1{\cdot}10^{18}$ cm^{-3}. A possible reason for this is a slightly higher growth temperature which leads in turn to a higher segregation of Sn and to a higher number of acceptor-like point defects. However, the values determined in this way allow the calculations of the Fermi level position in the intentionally undoped SiGeSn region according to Eq. (6).

Finally, the complete previously described method to calculate the indirect bandgap $E^L_{g,SiGeSn}$ out of the built-in voltage v_{bi} of the investigated pn^{++} junction was performed using the already shown findings and relationships. The final results for the indirect bandgap $E^L_{g,SiGeSn}$ are compared with the previously mentioned simulative results from Moontragoon, Soref and Ikonic [16] and continuative calculations from Sun, Soref and Cheng [23] in the summarizing graph in Fig. 11. As it can be seen, the bandgap of the samples *5.0Sn* and *10.0Sn* are remarkably smaller than both simulative results of Moontragoon, Soref and Ikonic [16] and Sun, Soref and Cheng [23], while the bandgap of sample *7.5Sn* fits almost perfectly to the simulative results of Sun, Soref and Cheng [23]. A possible explanation for this is the influence of the residual strain, as stated in Table 1 on the indirect bandgap of these SiGeSn alloys.

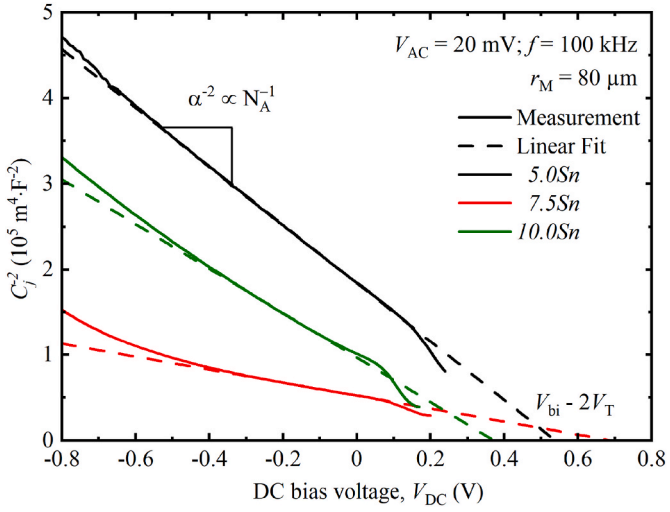

Fig. 8. C–$^{-2}$V characteristics of one SiGeSn pin diode for each composition.

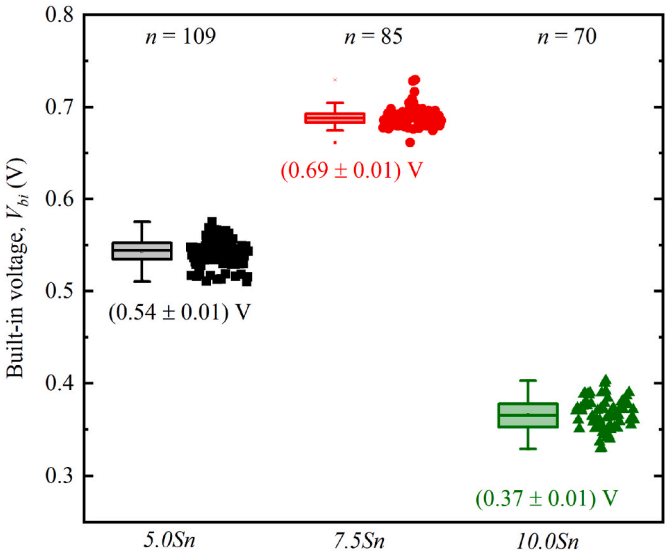

Fig. 9. Compositional dependence of the built-in voltages, extracted for at least $n \geq 70$ devices per alloy composition each.

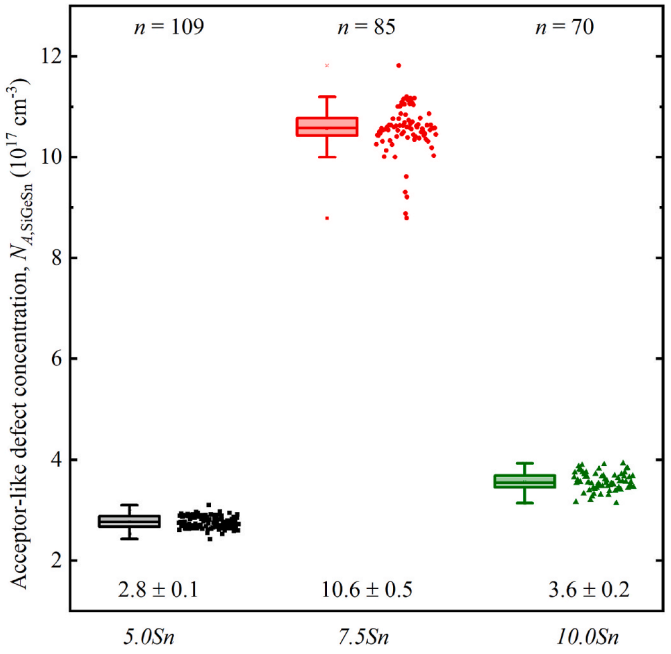

Fig. 10. Compositional dependence of the acceptor-like defect concentration in the intentionally undoped SiGeSn region, extracted for at least $n \geq 70$ devices per alloy composition each.

Another aspect, which is also not being covered by this investigation, is the influence of bandgap narrowing due to degenerate doping. The investigated pn^{++} junction is formed by the unintentionally p-type doped SiGeSn region and the highly n-type doped SiGeSn top layer, whose doping with $N_D = 5{\cdot}10^{19}$ cm^{-3} is already in the degenerated regime. This could be an explanation for the deviation between the experimental and the simulative results. However, the degenerated doping is necessary for the formation of an ohmic tunneling contact.

Besides that, it needs to be considered that both simulations consider some simplifications regarding the material parameter of the alloying elements Si, Ge, and Sn. Despite the deviations to simulative results, these experimental results for the indirect bandgap of SiGeSn, lattice matched to Ge are the first ever reported to the best of our knowledge.

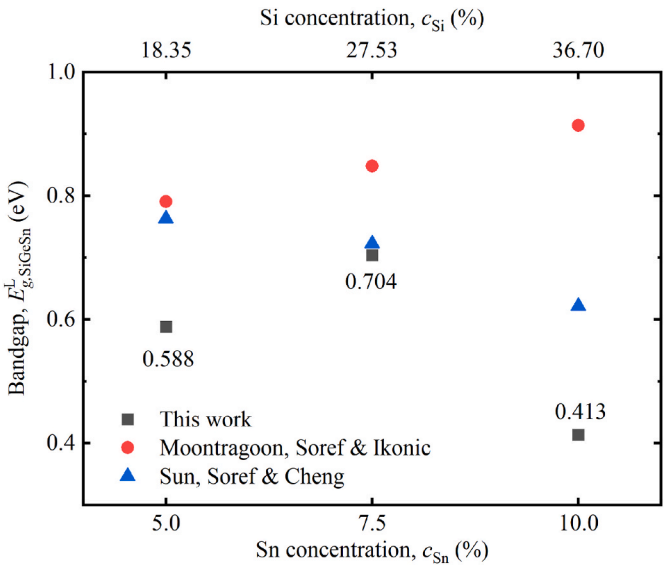

Fig. 11. Comparison of the extracted bandgap $E^L_{g,SiGeSn}$ with simulative re-sults from Moontragoon, Soref & Ikonic [16] and Sun, Soref & Cheng [23].

Furthermore, it can be stated that the different composition of the alloying elements Si, Ge and Sn has a significant influence on the indirect bandgap of their alloy. Compared with the values of the alloying elements Si ($E^L_{g,Si} = 2.0$ eV), Ge ($E^L_{g,Ge} = 0.66$ eV) and Sn ($E^L_{g,Sn} = 0.14$ eV) [23] the bandgap stays in the range of $0.413\ \text{eV} \leq E^L_{g,SiGeSn} \leq 0.704\ \text{eV}$.

6. Conclusion

We report the, to the best of our knowledge, first experimental results for the indirect bandgap of SiGeSn, lattice-matched on Ge. For this, SiGeSn pin diodes were grown via MBE and discrete devices were fabricated using a CMOS compatible single mesa process and subsequentially electrically characterized. The results of the CV intercept method and the consecutive calculation reveal a strong influence of the alloy composition on its bandgap. In fact, the bandgap is in the range of $E^L_{g,SiGeSn} = \{0.588, 0.704, 0.413\}$ eV for the respective alloy compositions of $c_{Sn} = \{5.0, 7.5, 10.0\}$ % at a constant ratio of Si/ Sn = 3.67.

CRediT authorship contribution statement

Daniel Schwarz: Writing – review & editing, Writing – original draft, Visualization, Validation, Methodology, Investigation, Formal analysis, Data curation, Conceptualization. **Erich Kasper:** Writing – review & editing, Validation. **Florian Bärwolf:** Writing – review & editing, Validation, Formal analysis, Data curation. **Ioan Costina:** Writing – review & editing, Validation, Supervision, Funding acquisition. **Michael Oehme:** Writing – review & editing, Validation.

Declaration of competing interest

The authors declare that they have no known competing financial interests or personal relationships that could have appeared to influence the work reported in this paper.

Data availability

Data will be made available on request.

Acknowledgements

The authors would like to thank for the funding of this work by the Bundesministerium für Bildung und Forschung (BMBF) within the scope of the project SiGeSn NanoFET (16ES1076).

References

[1] B. Marzban, L. Seidel, T. Liu, V. Kiyek, K. Wu, M.H. Zollner, et al., Electrically pumped SiGeSn microring lasers, in: 2022 IEEE Photonics Society Summer Topicals Meeting Series (SUM), Cabo San Lucas, IEEE, Mexico, 2022, https://doi.org/10.1109/SUM53465.2022.9858260, 1–1.
[2] N. von den Driesch, D. Stange, D. Rainko, I. Povstugar, P. Zaumseil, G. Capellini, et al., Advanced GeSn/SiGeSn group IV heterostructure lasers, Adv. Sci. 5 (2018) 1700955, https://doi.org/10.1002/advs.201700955.
[3] S. Wirths, D. Buca, Z. Ikonic, P. Harrison, A.T. Tiedemann, B. Holländer, et al., SiGeSn growth studies using reduced pressure chemical vapor deposition towards optoelectronic applications, Thin Solid Films 557 (2014) 183–187, https://doi.org/10.1016/j.tsf.2013.10.078.
[4] I.A. Fischer, A.S.M. Bakibillah, M. Golve, D. Hahnel, H. Isemann, A. Kottantharayil, et al., Silicon tunneling field-effect transistors with tunneling in line with the gate field, IEEE Electron. Device Lett. 34 (2013) 154–156, https://doi.org/10.1109/LED.2012.2228250.
[5] H. Wang, G. Han, X. Jiang, Y. Liu, J. Zhang, Y. Hao, Improved performance in GeSn/SiGeSn TFET by Hetero-line Architecture with Staggered tunneling junction, IEEE Trans Electron Devices 66 (2019) 1985–1989, https://doi.org/10.1109/TED.2019.2898328.
[6] D.J. Paul, The progress towards terahertz quantum cascade lasers on silicon substrates, Laser Photon. Rev. 4 (2010) 610–632, https://doi.org/10.1002/lpor.200910038.
[7] S.M. Sze, K.K. Ng, Physics of Semiconductor Devices, third ed., Wiley-Interscience, Hoboken, N.J, 2007.
[8] H. Kroemer, Heterostructure devices: a device physicist looks at interfaces, Surf. Sci. 132 (1983) 543–576, https://doi.org/10.1016/0039-6028(83)90561-7.
[9] D. Schwarz, H.S. Funk, M. Oehme, J. Schulze, Alloy Stability of Ge1−xSnx with Sn concentrations up to 17% utilizing low-temperature molecular beam epitaxy, J. Electron. Mater. 49 (2020) 5154–5160, https://doi.org/10.1007/s11664-020-08188-6.
[10] E. Kasper, M. Bauer, M. Oehme, Quantitative secondary ion mass spectrometry analysis of SiO 2 desorption during in situ heat cleaning, Thin Solid Films 321 (1998) 148–152.
[11] M. Oehme, J. Werner, M. Kaschel, O. Kirfel, E. Kasper, Germanium waveguide photodetectors integrated on silicon with MBE, Thin Solid Films 517 (2008) 137–139, https://doi.org/10.1016/j.tsf.2008.08.062.
[12] M. Oehme, J. Werner, M. Kaschel, O. Kirfel, E. Kasper, Germanium waveguide photodetectors integrated on silicon with MBE, Thin Solid Films 517 (2008) 137–139, https://doi.org/10.1016/j.tsf.2008.08.062.
[13] L. Vegard, Die Konstitution der Mischkristalle und die Raumfüllung der Atome, Z Physik 5 (1921) 17–26, https://doi.org/10.1007/BF01349680.
[14] W.C. Dunlap, R.L. Watters, Direct measurement of the dielectric constants of silicon and germanium, Phys Rev 92 (1953) 1396–1397, https://doi.org/10.1103/PhysRev.92.1396.
[15] R.E. Lindquist, A.W. Ewald, Optical constants of single-crystal gray tin in the infrared, Phys Rev 135 (1964) A191–A194, https://doi.org/10.1103/PhysRev.135.A191.
[16] P. Moontragoon, R.A. Soref, Z. Ikonic, The direct and indirect bandgaps of unstrained Si $_x$ Ge $_{1-x-y}$ Sn $_y$ and their photonic device applications, J. Appl. Phys. 112 (2012) 073106, https://doi.org/10.1063/1.4757414.
[17] G. Dresselhaus, A.F. Kip, C. Kittel, Cyclotron resonance of electrons and holes in silicon and germanium crystals, Phys Rev 98 (1955) 368–384, https://doi.org/10.1103/PhysRev.98.368.
[18] B.L. Booth, A.W. Ewald, Nonparabolicity of the gray-tin Γ 8 + conduction band, Phys Rev 168 (1968) 796–804, https://doi.org/10.1103/PhysRev.168.796.
[19] H.D. Barber, Effective mass and intrinsic concentration in silicon, Solid State Electron. 10 (1967) 1039–1051, https://doi.org/10.1016/0038-1101(67)90122-0.
[20] B.W. Levinger, D.R. Frankl, Cyclotron resonance measurements of the energy band parameters of germanium, J. Phys. Chem. Solid. 20 (1961) 281–288, https://doi.org/10.1016/0022-3697(61)90015-4.
[21] S.H. Groves, C.R. Pidgeon, A.W. Ewald, R.J. Wagner, Interband magnetoreflection of α-Sn, J. Phys. Chem. Solid. 31 (1970) 2031–2049, https://doi.org/10.1016/0022-3697(70)90006-5.
[22] G. Chen, Y. Yu, Y. Shi, N. Li, W. Luo, L. Cao, et al., High-speed photodetectors on silicon photonics platform for optical interconnect, Laser Photon. Rev. 16 (2022) 2200117, https://doi.org/10.1002/lpor.202200117.
[23] G. Sun, R.A. Soref, H.H. Cheng, Design of an electrically pumped SiGeSn/GeSn/SiGeSn double-heterostructure midinfrared laser, J. Appl. Phys. 108 (2010) 033107.